Pursuit of Stability, Electronic, Lattice Dynamics, and Thermoelectric Properties of Half Heusler Compound TiFeSe

Prakash Khatri[1, 2, *]

[1]Central Department of Physics, Tribhuvan University, Kirtipur 44613, Kathmandu, Nepal
[2]Department of Physics, Tribhuvan University, Siddhanath Science Campus, Mahendranagar 10406, Nepal

Research Article

ABSTRACT

Half-Heusler (HH) compounds are increasingly popular for their use as thermoelectric materials in high-temperature applications. The present work explores the electron and phonon transport properties of TiFeSe compounds to understand their thermoelectric behaviour using Density Functional Theory (DFT), semiclassical Boltzmann transport equation, and Slack's equation. The compound is thermodynamically, dynamically, and mechanically stable, exhibiting non-magnetic semiconductor behaviour with an indirect bandgap of 0.80 eV. The compound has a higher Young's modulus and bulk modulus, indicating better mechanical strength, and also has a high melting point, as calculated from the elastic constants. The lattice thermal conductivity is 24.84 $Wm^{-1}K^{-1}$ at room temperature and decreases as the temperature increases. The maximum power factor (PF) in the compound for hole doping is 182 $\mu W/cmK^2$, leading to a maximum figure of merit (zT) value of 1.45 at 1200 K. This study shows that the hole-doped TiFeSe compound is a promising candidate for high-temperature power generation in thermoelectric applications.

1. INTRODUCTION

The growing gap between the global energy demand and limited supply of non-renewable resources is pushing us toward an energy crisis. Outdated energy policies, weak regulatory standards, and lack of proper energy storage are all intensifying the crisis. To alleviate these issues, many researchers are actively working to find solutions. One way to reduce the crisis is by turning waste heat from industries, transportation vehicles etc into useful electricity using thermoelectric materials [1-4]. Nowadays, these materials are a key part of modern technology, and their conversion efficiency depends on the parameter thermodynamic figure of merit that can be expressed as [5, 6]:

$$zT = \frac{S^2 \sigma T}{\kappa_{el} + \kappa_l} .... (i)$$

Where S, σ, κ_{el}, κ_l, and T are the Seebeck coefficient, electrical conductivity, electronic and lattice contributions to thermal conductivity, and absolute temperature, respectively. The interdependence of S, σ, and κ_{el}, along with electron-phonon coupling in crystals, limits the zT < 1 in many thermoelectric materials. However, a zT > 1 is needed for better energy conversion in thermoelectric devices [7, 8].

Although skutterudites [9] and chalcogenides [10] materials are better suited for medium temperature thermoelectric applications, skutterudites face thermal stability issues at high temperatures, and chalcogenides have weaker mechanical strength [11]. Thus, the half-Heusler (hH) materials are now a major focus in recent research for high-temperature thermoelectric applications because of their tunable electronic properties, excellent thermal stability, and mechanical strength [11, 12]. They are ternary intermetallics with a cubic MgAgAs-type structure and formula XYZ, where X and Y are transition metals, and Z is a main group element. They consist of three interpenetrating face-centered cubic (fcc) sublattices, with X, Y, and Z atoms occupying Wyckoff positions 4a (0, 0, 0), 4b (1/2, 1/2, 1/2), and 4c (1/4, 1/4, 1/4) positions respectively [13, 14]. The semiconducting ground state in hH alloys necessitates a nonmagnetic ground state due to the Slater-Pauling rule, which states that magnetic moment $\mu = (N_V - 18)$, where N_V is the valence electron count (VEC) per formula unit [15]. Since the magnetic moment vanishes for compounds with 18 VEC, the search for 18-VEC compounds leads us to the TiFeSe compound. This compound is reported to have a hH phase in the material project [16]. Furthermore, Nenuwe et al. [17] reported the stability, magnetic, mechanical, and thermoelectric properties of FeTiSe, but the zT value was calculated based solely on electronic thermal conductivity (κ_{el}). However, in hH compounds, lattice thermal conductivity (κ_l) is typically high due to their simple and symmetric crystal structure, as well as the fewer atoms in the primitive unit cell [18] and therefore cannot be neglected in thermal conductivity calculations. In this work, we used first-principles calculations to determine the transport parameters and their variations with chemical potential at different temperatures for both electron- and hole-doped TiFeSe compounds.

The paper is organized as follows: Section 2 covers the computational details, Section 3 includes the results and discussions, and Section 4 presents the conclusions of the study.

2. COMPUTATIONAL DETAILS

The structural, electronic, and magnetic properties were computed using density functional theory (DFT) implemented in Quantum ESPRESSO (QE) software version 7.1 [19]. Perdew, Burke, and Ernzerhof generalized gradient approximation (PBE-GGA) [20], is used to describe the exchange and correlation interactions. Ultrasoft pseudopotentials (USPP) were used for all elements with the valence electronic configurations as: Ti: $3s^2 3p^6 3d^2 4s^2$, Fe: $3s^2 3p^6 3d^6 4s^2$, and Se: $4s^2 4p^4$. The geometric visualization of the optimized crystal structure is done with

XcrySDen [21]. The calculations used a plane wave basis with a kinetic energy cut-off of 70 Ry and a charge density cut-off of 700 Ry. A Monkhorst-Pack [22] k-point grid of 10×10×10 in the first irreducible Brillouin zone (BZ) was used for integrating over the BZ. Diagonalization (David), a mixing beta factor (0.3), and Marzari-Vanderbilt smearing [23] (width 0.005 Ry) were used throughout the calculations. $\Gamma \to X \to W \to K \to \Gamma \to L \to U \to W \to L \to K$ is the high symmetry path in the first BZ along which sampling points are chosen. A denser k-point mesh of 20 × 20 × 20 was used to evaluate the density of states (DOS) and partial density of states (PDOS). The energy eigenvalues calculated using DFT with the same mesh were also used in the calculations within the BoltzTraP code to estimate the transport coefficients by solving the Boltzmann transport equations [24]. Phonon dispersion calculations were carried out to evaluate dynamical stability using density functional perturbation theory (DFPT) [25] within the Quantum ESPRESSO package, with a 2 × 2 × 2 q-point mesh. The mechanical properties were assessed using the thermo_pw [26] tool within QE suite, while Slack's equation [27] was used to calculate the κ_l.

3. RESULTS AND DISCUSSION
3.1. Structural Stability

.

Before studying the properties properties, it's important to ensure its stability for any hypothetical compounds. TiFeSe is a ternary hH compound that belongs to the $F\bar{4}3m$ space group and has a structure of MgAgAs prototype. In XYZ hH compounds, the Y element stays at the 4b position, while the X and Z elements can occupy in the positions 4a and 4c. We have evaluated the stability by placing Fe at the 4b site and assessed the suitability of Ti and Se by swapping their positions at the 4a and 4c sites. The labels I and II refer to the two structural configurations as in Figs.1(a) and 1(b) that differ in their atomic positions, as shown in Table 1. The energy vs. volume plots Figs.1(c) and 1(d) for the I and II structures are fitted using the Murnaghan equation of state [28] to obtain the optimized lattice parameter. After VC-relax, it results in lattice parameters of 10.60 a.u. and 10.59 a.u. for the type I and type II structures, respectively. Based on the SCF energy, the type I structure has a slightly lower total energy (−395.373480 Ry) compared to that (−395.373472 Ry) of type II structure. Although the energy difference is not significant, we have selected the slightly lower-energy structure (Type I) for our calculations, which is also reported in Ref. [17]. The calculated lattice parameter is in close agreement with the reported value of 10.62 a.u. (5.62 Å) in Ref. [17]. Therefore, all further calculations were carried out using the type I structure
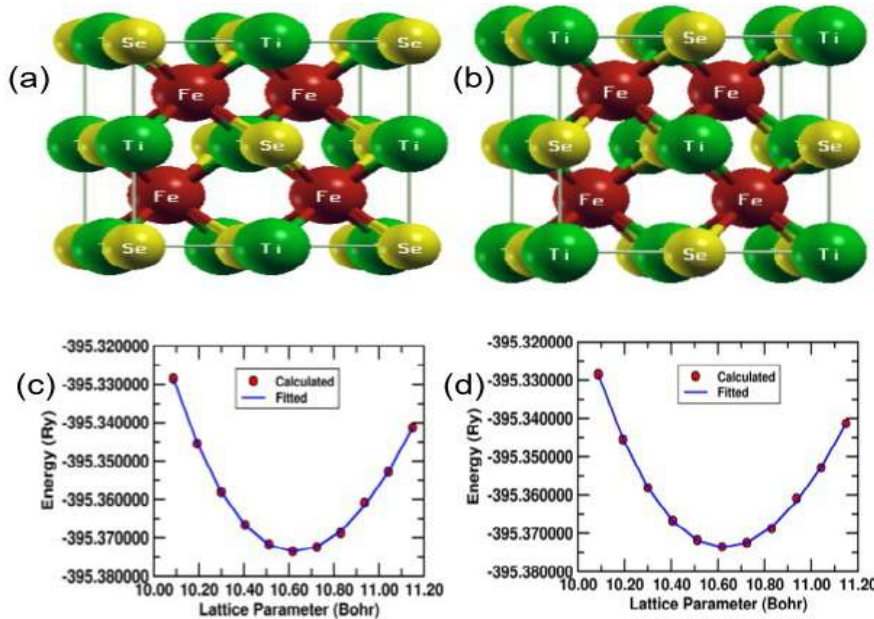
Fig. 1. (a) Conventional unit cell of TiFeSe (type-I) (b) Conventional unit cell of TiFeSe (type-II) (c) Energy (in Ry) vs. lattice parameter (in Bohr) for TiFeSe (type-I) (d) and Energy (in Ry) vs. lattice parameter (in Bohr) for TiFeSe (type-II)).

After structural optimization, we confirmed the compound's thermodynamic, dynamical, and mechanical stability by calculating the formation energy, phonon dispersion, and elastic constants, respectively. The formation energy is calculated as:

$$E_{form} = \frac{(E_{TiFeSe})-(xE_{Ti}+yE_{Fe}+zE_{Se})}{x+y+z}$$ .... (ii)

Here, E_{TiFeSe}, E_{Ti}, E_{Fe}, and E_{Se} represent the total energy p.u.c. of the bulk crystal TiFeSe, bulk elements Ti, Fe, and Se, respectively, x, y, and z are the total number of Ti, Fe, and Se atoms, respectively. From our calculations, the formation energy of TiFeSe is −0.54 eV/atom. The stability of the materials against elemental segregation is suggested by this negative formation energy.

Table 1. Atomic positions, optimized lattice parameters (in a.u.) and total energy (Ry) for type (I and II) of TiFeSe.

Type	4a (X)	4b (Y)	4c (Z)	Lattice Parameter (a.u.)	Total energy (Ry)
I	0, 0,0	0.25, 0.25, 0.25	0.5, 0.5, 0.5	10.60	−395.373480
II	0.5, 0.5, 0.5	0.25, 0.25, 0.25	0, 0, 0	10.59	−395.373472
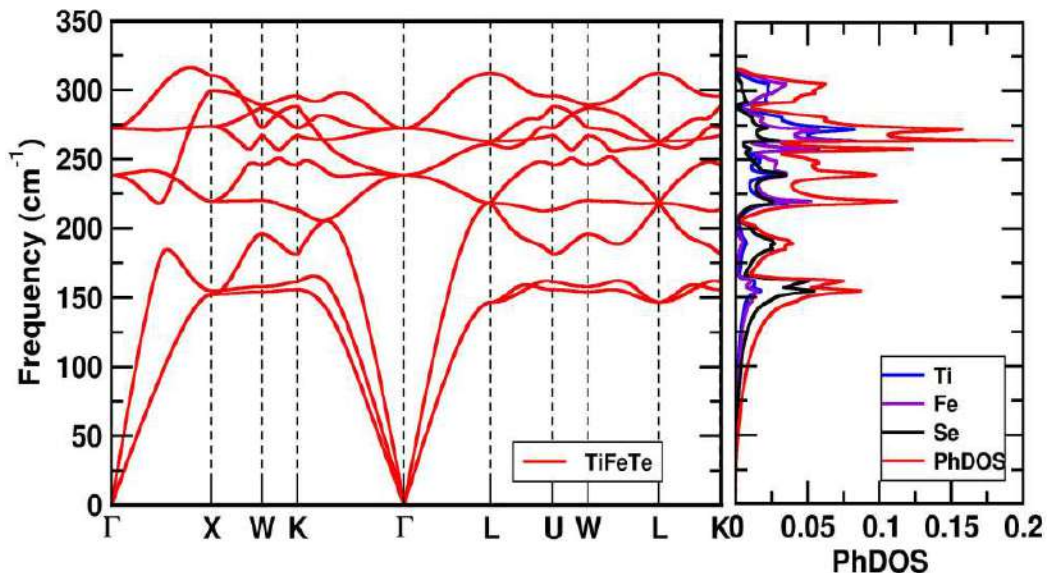
Fig. 2. Phonon dispersion plot and phonon density of states (PhDOS) of TiFeSe.

The phonon dispersion along the specified high-symmetry points is presented alongside the phonon density of states (PhDOS) in the Fig 2. This is used to check the dynamical stability of the compound. Since TiFeSe has three atoms in its primitive cell, the dispersion plot has nine vibrational modes, three low frequency acoustic modes and six high frequency optical modes. The absence of imaginary frequencies indicates dynamical stability of the compound. The acoustic branches are highly dispersive and are almost linear near the Γ point, resulting in higher group velocities, while the optical modes are flatter and have lower group velocities. This makes acoustic modes more dominant in heat transfer than optical modes. The high frequencies are mainly due to the vibration of Fe and Ti atoms having nearly similar atomic masses and the low-frequency branches are caused by the vibrations of relatively heavier Se atoms, as seen in the PhDOS. The overlap between low-frequency optical modes and high-frequency acoustic modes suggests strong phonon-phonon scattering, which affects the lattice thermal conductivity of the compound.

The mechanical stability of the compound is evaluated by calculating the elastic constants with the thermo_pw code [26] in Quantum ESPRESSO. The cubic materials have three independent elastic constants: C_{11}, C_{12}, and C_{44}, which were found to be 267.45 GPa, 101.38 GPa, and 74.77 GPa, respectively. The compound meets the Born's mechanical stability criteria [29] ($C_{11} > 0$, $C_{44} > 0$, $C_{11} - C_{12} > 0$, and $C_{11} + 2C_{12} > 0$). The Young's modulus and bulk modulus are calculated using the Voigt-Reuss-Hill approximation [30]. The ratio of stress to strain defines Young's modulus, which quantifies a material's stiffness. With a Young's modulus of 200.64 GPa, the compound exhibits the significant rigidity. The bulk modulus (B) measures how compressible a material is

under pressure. TiFeSe has a high B value of 156.73 GPa, means that it resists compression and performs well under high pressure. The melting temperature (T_m) of cubic crystals can be calculated from elastic constant C_{11} using the formula [31]:

$$T_m = [553 \text{ K} + (5.91 \text{ K / GPa}) \, C_{11}] \pm 300 \text{ K} \dots\dots\dots\dots\dots \text{(iii)}$$

The compound's high melting point of 2133.62 K suggests it is well-suited for high-temperature applications.

3.2. Electronic and magnetic properties

The electronic band structures (EBS), along with the DOS and PDOS, computed using the optimized lattice parameters, are displayed in Fig 3. The high-symmetry path Γ → X → W → K → Γ → L → U → W → L → K is used for plotting EBS and a dashed line at 0 eV represents the Fermi energy. The valence band maximum (VBM) is located at the L point, and the conduction band minimum (CBM) at the Γ point. This indicates that TiFeSe is an indirect band gap semiconductor with a band gap of 0.80 eV. The calculated band gap value is very closer to (0.81 eV) as reported by Nenuwe et al. [17], but lower than the value (0.86 eV) found in the Materials Project [16]. Variations in band gap values may arise due to the use of different exchange-correlation functionals in the studies. Additionally, there is no experimental band gap value available for comparison.

The VBM at the L point is a doubly degenerate state with heavy-hole and light-hole bands of varying curvatures. Sharp bands with higher curvature exhibit a smaller effective mass, whereas the flat bands with lower curvature result a larger effective mass for their charge carriers. Thus, the degenerate bands at the VBM results in a higher Seebeck coefficient for hole doped compounds. There is a triply degenerate band at the Γ point, ~ 360 meV below the VBM, while the band extrema at the X point of the CB is ~290 meV higher than the CBM. These bands do not significantly contribute to the

transport properties of the compounds. The symmetrical DOS plot between the spin-up and spin-down channels indicates the non-magnetic nature of the material. The PDOS plot reveals that the Fe-3d orbitals contribute significantly the VB, while Ti-3d orbitals dominate the CB, with minimal contributions from Se-4p orbitals in both bands. TiFeSe is a

non-magnetic semiconductor with zero magnetic moment 0.0 μ_B and is consistent with the Slater-Pauling rule [15], magnetic moment $\mu = (Z - 18) \mu_B$, based on its valence electron count Z. The suitable semiconducting EBS and non-magnetic ground state of the compound motivate us to quantify the transport parameters and thermoelectric properties.
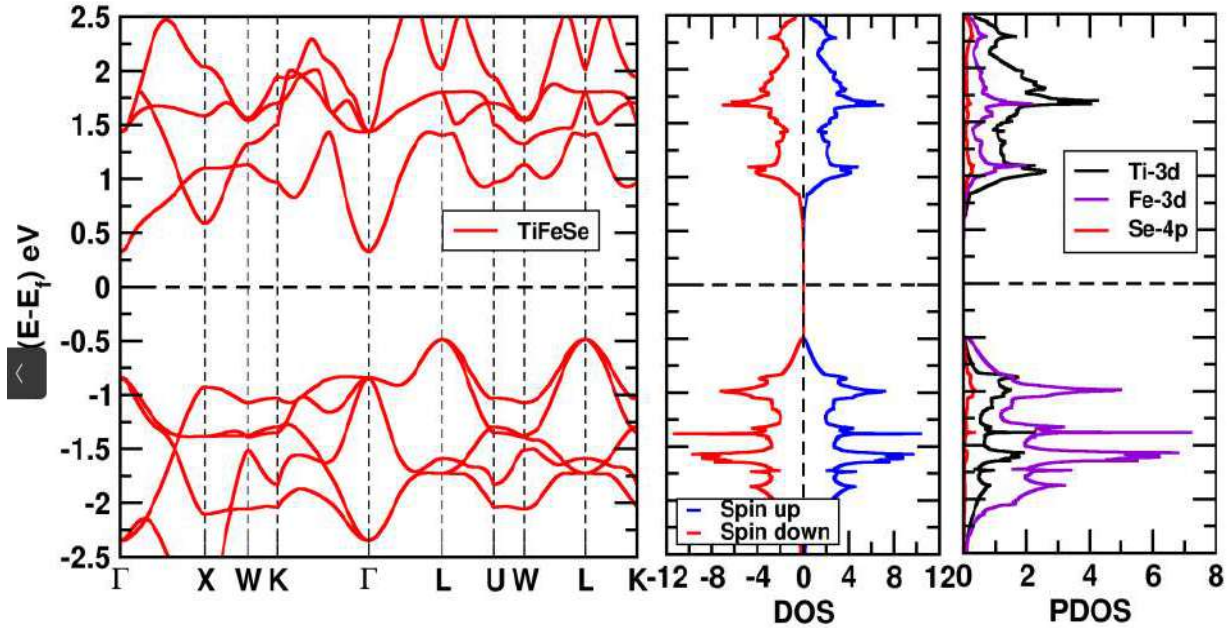

Fig. 3. The electronic band structure (EBS), total density of states (DOS), and partial density of states (PDOS) plots of TiFeSe atoms with a horizontal dotted line representing the Fermi level.

3.3. Thermoelectric Properties

The transport parameters, Seebeck coefficient (S), electrical conductivity (σ), and electronic thermal conductivity (κ_{el}) are calculated using the semi-classical Boltzmann transport theory in BoltzTraP software [24]. It relies on the rigid band approximation (RBA) and the constant relaxation time approach (CRTA). A constant relaxation time of 10^{-14} seconds chosen based on some other hH compounds, is used to evaluate the transport properties as a function of chemical potential for different temperatures, as shown in Fig. 4.

Mott's equation [32] for the Seebeck coefficient:

$S = \frac{8\pi^2 k_B^2 m_D T}{3eh^2}\left(\frac{\pi}{3n}\right)^{1/3}$ ....(iv)

shows that S depends on the DOS effective mass (m_{DOS}) and higher carrier concentration (n). The DOS effective mass $m_{DOS} = N_v^{2/3} m_b$, depends on the total band degeneracy N_v.

The Fig. 4(a) shows that for both p-type (hole doping) and n-type (electron doping) rise until they reach a peak value as the chemical potential (μ) increases. S peaks in the chemical potential (μ) range of − 0.2 eV to 0.2 eV for all temperatures. With further increases in the μ, S rapidly decreases after reaching the peak value. The peak value of S for p-type regions (hole doping) is higher than for n-type regions (electron doping) at all temperatures. The peak S is ~ 1120 µV/K for p-type regions and ~915 µV/K for n-type regions at 400 K within the observed range of μ. The higher S in the p-type region may result from the doubly degenerate band at the VBM. However, a triply degenerate band at the Γ point,

~360 meV below the VBM, does not have a significant effect on the transport parameters. The band curvature around the CBM is relatively sharper, leading to a lower S for electrons in the n-type regions. The closest band extrema to CBM is at the X point, ~ 290 meV higher than the CBM, and does not make a major contribution to the transport properties. The carrier concentration increases and hence peak value of S decreases as the temperature rises. At 1200 K, the peak values of the S are ~ 445 µV/K for p-type and ~350 µV/K for n-type TiFeSe compounds. The maximum values of S for TiFeSe in this study are comparable to those observed in LiCaX (X = As, Sb) [33], but they are lower than those reported for XFeTe (X = Ti, Hf) [34] systems at the same temperature.

The relationship between electrical conductivity (σ) and chemical potential (μ) at different temperatures is illustrated in Fig.4(b). σ exhibits a similar pattern at all temperatures. In the μ range of −0.2 to 0.2 eV, σ remains nearly zero, but it rises outside of this range for all temperatures. When the temperature increases, electrons gain thermal energy, which boosts their mobility μ_c and leads to higher electrical conductivity (σ = $ne\mu_c$). σ is higher for hole doping (negative μ) than for electron doping (positive μ) region, indicating that p-type doping demonstrates greater σ compared to n-type doping within the examined region. However, this trend could alter if the temperature-dependent relaxation time, calculated from the effective mass, is included in the calculation of σ. Fig.4(d) illustrates that the electronic thermal conductivity (κ_{el}), increases with rising temperature. The Wiedemann-Franz law ($\kappa_{el} = L\sigma T$, where L is the Lorentz number) relates σ to κ_{el}. κ_{el} displays a similar trend in variation with μ as σ does across different temperatures.

4

The change in the power factor (PF = S²σ) with the μ at different temperatures is illustrated in Fig.4(c). The PF has very low values close to the Fermi level; however, it rises sharply with an increase in μ. There are two distinct peaks in the PF for both p-type and n-type materials. As the μ continues to increase, the PF gradually decreases, and this trend is obeyed across all temperatures. The peak PF is 53 μW/cmK² for n-type doping and 46 μW/cmK² for p-type doping at 400 K. As the temperature increases, the peak value

of the PF rises due to enhanced σ, despite a decline in the S. TiFeSe exhibits its highest PF values of 182 μW/cmK² for p-type doping and 161 μW/cmK² for n-type doping at a temperature of 1200 K. p-type doping has higher PF values at all temperatures compared to n-type doping. The calculated PF values are slightly lower than those previously reported for 18 VEC hH TiIrX (X = As and Sb) at 600 K [35]. These PF values indicate better thermoelectric performance at elevated temperatures.
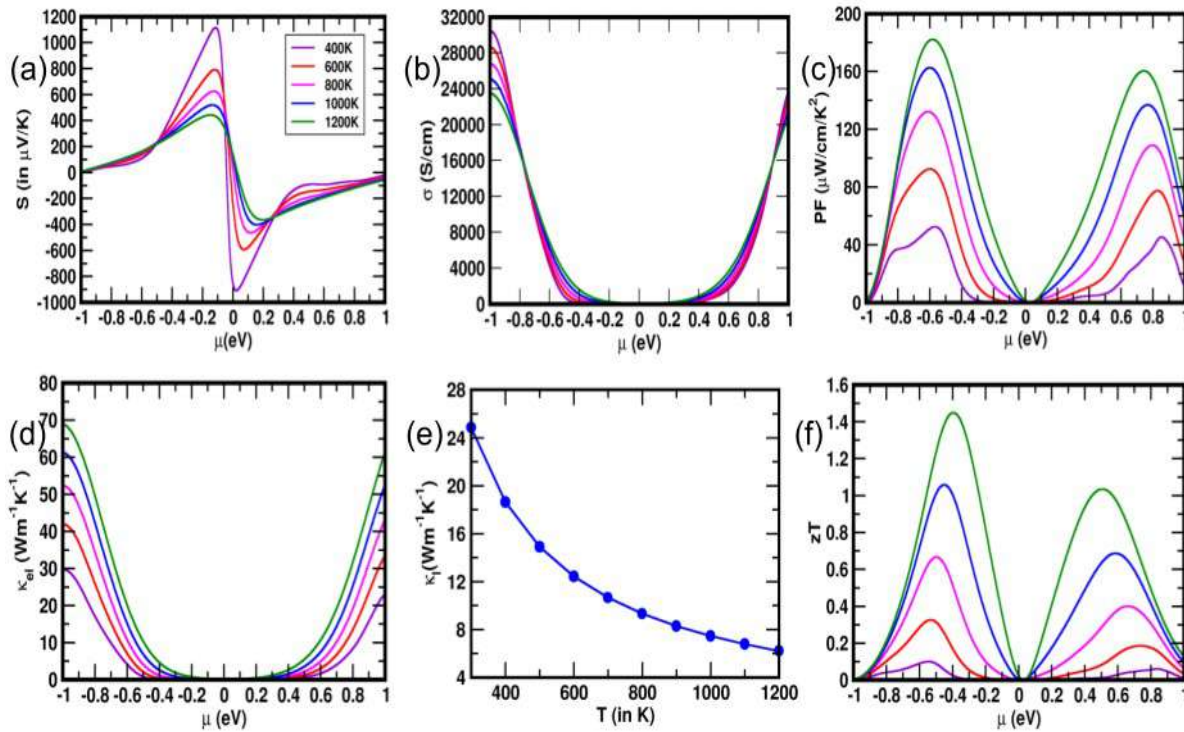
Fig. 4. Variations of (a-d) Seebeck coefficient, electrical conductivity, power factor, and electronic thermal conductivity with respect to chemical potential; (e) lattice thermal conductivity as a function of temperature; and (f) zT with chemical potential at different temperatures.

Fig.4(e) shows the calculated κ_l from Slack's equation of TiFeSe as a function of temperature. The Slack's equation is [27],

$$\kappa_l = \frac{V^{1/3} A M \theta_D^3}{\gamma^2 T n^{2/3}} \quad \text{......................(v)}$$

where, Grüneisen parameter is calculated as,

$$\gamma = \frac{9 - 12(v_t/v_l)^2}{2 + 4(v_t/v_l)^2} \quad \text{...................(vi)}$$

and dimensionless constant,

$$A = \frac{2.43 \times 10^{-8}}{1 - 0.514/\gamma + 0.228/\gamma^2} \text{......................(vii)}$$

M, V, and n represent the average atomic mass, the volume per cell, and the number of atoms in the primitive unit cell, respectively. The Debye temperature (456.24 K) and the Grüneisen parameter (1.69) are obtained from the longitudinal velocity (v_l) of (6158.954 m/s) and the transverse velocity (v_t) of (3368.264 m/s), which are calculated from the elastic constants using the thermo_pw code.

The κ_l at room temperature is 24.84 Wm⁻¹K⁻¹. Phonon generated by lattice vibrations, whose scattering increases with temperature in crystalline materials, influence the κ_l. κ_l decreases with increasing temperature, and reaches its minimum value of 6.21 Wm⁻¹K⁻¹ at 1200 K. The κ_l value of the compound in this study at 300 K is much higher than that of

the iron-based 18 VEC hH NbFeTe [36], slightly more than NbFeSb [37], close to TiFeTe, and lower than HfFeTe [34].

The variation in the zT as a function of μ for different temperatures is displayed in the Fig.4(f). Like PF, the zT has very low values close to the Fermi level and further rises sharply with an increase in μ both sides making two distinct peaks in the zT for both hole and electron doped materials. At 400 K, the peak zT values are 0.11 for hole doped and 0.07 for electron doped compounds. As the temperature increases, the peak value of zT also rises, reaching 1.45 for the p-type region and 1.04 for the n-type region at 1200 K. Thus, the present compound shows better potential for thermoelectric applications at high temperatures in hole-doped materials compared to electron-doped ones. These zT values are significantly lower than those reported by Nenuwe et al. [17], which did not consider the lattice contribution to thermal conductivity. Thus, it indicates that the lattice contribution cannot be neglected in zT calculations for hH compounds. The zT calculated for TiFeSe is lower than that of TiFeTe [34] but higher than that of NbFeTe [36], considering the temperature-dependent relaxation time.

By utilizing the band engineering for electronic transport and phonon scattering strategies for thermal transport, the zT of

the compounds can be further enhanced.

4. CONCLUSIONS

In conclusion, this study summarizes the key findings from the theoretical investigation of TiFeSe compounds, based on density functional theory and semiclassical Boltzmann transport theory. The thermodynamic, dynamic, and mechanical stabilities of the TiFeSe compound were assessed through the evaluation of formation energy, phonon spectrum, and elastic constants, respectively. The EBS and DOS indicate that the compound exhibits non-magnetic semiconducting behaviour with indirect band gap of 0.80 eV. The κ_l calculated using Slack's equation, is 24.84 $Wm^{-1}K^{-1}$ at room temperature and was found to decrease with increasing temperature. The electronic and thermal transport properties were evaluated at various chemical potentials and temperatures. TiFeSe achieves a maximum zT value of 1.45 for hole doping and 1.04 for electron doping, respectively, at 1200 K. The high PF of the compound contributes zT > 1. The zT values suggest that TiFeSe is a strong candidate for thermoelectric performance and this study will assist in guiding experimental work.

REFERENCES

[1] S. Lv, Z. Qian, D. Hu, X. Li, W. He, A comprehensive review of strategies and approaches for enhancing the performance of thermoelectric module, *Energies*, 13 (2020) 3142. https://doi.org/10.3390/en13123142.

[2] P. Rodgers, Silicon goes thermoelectric, *Nature Nanotechnology*, 3 (2008) 76. https://doi.org/10.1038/nnano.2008.17.

[3] J. Tervo, A. Manninen, R. Ilola, H. Hänninen, State-of-the-art of thermoelectric materials processing, *VTT Technical Research Center of Finland*, Vuorimiehentie (2009).

[4] C. Gayner, K. K. Kar, Recent advances in thermoelectric materials, *Progress in Materials Science*, 83 (2016) 330-382. https://doi.org/10.1016/j.pmatsci.2016.07.002.

[5] G. J. Snyder, E. S. Toberer, Complex thermoelectric materials, *Nature Materials*, 7 (2008) 105-114. https://doi.org/10.1038/nmat2090.

[6] M. Wambach, R. Stern, S. Bhattacharya, P. Ziolkowski, E. Müller, G. K. Madsen, A. Ludwig, Unraveling self-doping effects in thermoelectric TiNiSn half-Heusler compounds by combined theory and high-throughput experiments, *Advanced Electronic Materials*, 2 (2016) 1500208. https://doi.org/10.1002/aelm.201500208.

[7] J. R. Sootsman, D. Y. Chung, M. G. Kanatzidis, New and old concepts in thermoelectric materials, *Angewandte Chemie International Edition*, 48 (2009) 8616-8639. https://doi.org/10.1002/anie.200900598.

[8] J. Wei, L. Yang, Z. Ma, P. Song, M. Zhang, J. Ma, X. Wang, Review of current high-ZT thermoelectric materials, *Journal of Materials Science*, 55 (2020) 12642-12704. https://doi.org/10.1007/s10853-020-04949-0.

[9] C. Uher, Skutterudites: Prospective novel thermoelectrics, in *Semiconductors and Semimetals*, 69 (2001) 139-253. https://doi.org/10.1016/S0080-8784(01)80151-4.

[10] Y. Shi, C. Sturm, H. Kleinke, Chalcogenides as thermoelectric materials, *Journal of Solid State Chemistry*, 270 (2019) 273-279. https://doi.org/10.1016/j.jssc.2018.10.049

[11] L. Huang, Q. Zhang, B. Yuan, X. Lai, X. Yan, Z. Ren, Recent progress in half-Heusler thermoelectric materials, *Materials Research Bulletin*, 76 (2016) 107-112. https://doi.org/10.1016/j.materresbull.2015.11.032

[12] S. J. Poon, Recent advances in thermoelectric performance of half-Heusler compounds, *Metals*, 8 (2018) 989. https://doi.org/10.3390/met8120989

[13] F. Casper, T. Graf, S. Chadov, B. Balke, C. Felser, Half-Heusler compounds: novel materials for energy and spintronic applications, *Semiconductor Science and Technology*, 27 (2012) 063001. http://dx.doi.org/10.1088/0268-1242/27/6/063001

[14] A. Page, P. F. P. Poudeu, C. Uher, A first-principles approach to half-Heusler thermoelectrics: Accelerated prediction and understanding of material properties, *Journal of Materiomics*, 2 (2016) 104-113. https://doi.org/10.1016/j.jmat.2016.04.006

[15] I. Galanakis, P. Mavropoulos, P. H. Dederichs, Electronic structure and Slater–Pauling behaviour in half-metallic Heusler alloys calculated from first principles, *Journal of Physics D: Applied Physics*, 39 (2006) doi:10.1088/0022-3727/39/5/S01

[16] Materials Project, TiFeSe (mp-961660). https://next-gen.materialsproject.org/materials/mp-961660, 2024. (accessed 08 October 2024).

[17] N. O. Nenuwe, N. O. Agbawe, Ab initio predictions of thermoelectric, mechanical, and phonon characteristics of FeTiSe half-Heusler compound, *Current Applied Physics*, 53 (2023) 132-141. https://doi.org/10.1016/j.cap.2023.06.008.

[18] S. Anand, M. Wood, Y. Xia, C. Wolverton, G. J. Snyder, Double half-Heuslers, *Joule*, 3 (2019) 1226-1238. https://doi.org/10.1016/j.joule.2019.04.003.

[19] P. Giannozzi, O. Andreussi, T. Brumme, O. Bunau, M. B. Nardelli, M. Calandra, S. Baroni, Advanced capabilities for materials modelling with Quantum ESPRESSO, *Journal of Physics: Condensed Matter*, 29 (2017) 465901. https://doi.org/10.1088/1361-648X/aa8f79.

[20] J. P. Perdew, K. Burke, M. Ernzerhof, Generalized gradient approximation made simple, *Physical Review Letters*, 77 (1996) 3865. https://doi.org/10.1103/PhysRevLett.77.3865.

[21] A. Kokalj, XCrySDen—a new program for displaying crystalline structures and electron densities, *Journal of Molecular Graphics and Modelling*, 17 (1999) 176-179. https://doi.org/10.1016/S1093-3263(99)00028-5.

[22] H. J. Monkhorst, J. D. Pack, Special points for Brillouin-zone integrations, *Physical Review B*, 13 (1976) 5188. https://doi.org/10.1103/PhysRevB.13.5188.

[23] N. Marzari, D. Vanderbilt, A. De Vita, M. C. Payne, Thermal contraction and disordering of the Al (110) surface, *Physical Review Letters*, 82 (1999) 3296. https://doi.org/10.1103/PhysRevLett.82.3296

[24] G. K. Madsen, J. Carrete, M. J. Verstraete, BoltzTraP2, a program for interpolating band structures and calculating semi-classical transport coefficients, *Computer Physics Communications*, 231 (2018) 140-145. https://doi.org/10.1016/j.cpc.2018.05.010.

[25] S. Baroni, S. De Gironcoli, A. Dal Corso, P. Giannozzi, Phonons and related crystal properties from density-functional perturbation theory, *Reviews of Modern Physics*, 73 (2001) 515. https://doi.org/10.1103/RevModPhys.73.515.

[26] A. D. Corso, thermo_pw. http://dalcorso.github.io/thermo_pw, 2024 (accessed 08 October 2024).

[27] D. T. Morelli, G. A. Slack, High lattice thermal conductivity solids, in *High Thermal Conductivity Materials*, Springer New York, 2006. (pp. 37-68).

[28] F. D. Murnaghan, The compressibility of media under extreme pressures, *Proceedings of the National Academy of Sciences*, 30 (1944) 244-247. https://doi.org/10.1073/pnas.30.9.244.

[29] M. Born, R. Fürth, The stability of crystal lattices. III: An attempt to calculate the tensile strength of a cubic lattice by purely static considerations, in Mathematical Proceedings of the Cambridge Philosophical Society, 36 (1940) 454-465. https://doi.org/10.1017/S0305004100017503.

[30] L. I. A. N. G. Zuo, M. I. C. H. E. L. Humbert, C. L. A. U. D. E. Esling, Elastic properties of polycrystals in the Voigt-Reuss-Hill approximation, *Journal of Applied Crystallography*, 25 (1992) 751-755. https://doi.org/10.1107/S0021889892004874

[31] M. E. Fine, L. D. Brown, H. L. Marcus, Elastic constants versus melting temperature in metals, *Scripta Metallurgica*, 18 (1984) 951-956.

https://doi.org/10.1016/0036-9748(84)90267-9.

[32] G. Tan, L. D. Zhao, M. G. Kanatzidis, Rationally designing high-performance bulk thermoelectric materials, *Chemical Reviews*, 116 (2016) 12123-12149. https://doi.org/10.1021/acs.chemrev.6b00255.

[33] M. Singh, Augmented thermoelectric performance of LiCaX (X= As, Sb) Half Heusler compounds via carrier concentration optimization, *Journal of Physics and Chemistry of Solids,* 174 (2023) 111182. https://doi.org/10.1016/j.jpcs.2022.111182.

[34] P. Khatri, N. P. Adhikari, Mechanical and thermoelectric response of 18-valence electron half-Heusler tellurides XFeTe (X = Ti, Hf): A theoretical perspective, *Materials Today Communications,* 39 (2024) 108853. https://doi.org/10.1016/j.mtcomm.2024.108853.

[35] S. Chibani, O. Arbouche, M. Zemouli, K. Amara, Y. Benallou, Y. Azzaz, ... & M. Ameri, Ab initio prediction of the structural, electronic, elastic, and thermoelectric properties of half-Heusler ternary compounds TiIrX (X = As and Sb), *Journal of Electronic Materials*, 47 (2018) 196-204. https://doi.org/10.1007/s11664-017-5761-9.

[36] G. S. AlGhamdi, A. Saini, A. A. AlShaikhi, & R. Kumar, First-principles investigation of thermoelectric properties of half-Heusler alloy NbFeTe, *Journal of Superconductivity and Novel Magnetism,* (2021) 1-10. https://doi.org/10.1007/s10948-021-06082-8.

[37] T. Fang, S. Zheng, T. Zhou, L. Yan, & P. Zhang, Computational prediction of high thermoelectric performance in p-type half-Heusler compounds with low band effective mass, *Physical Chemistry Chemical Physics,* 19 (2017) 4411-4417. https://doi.org/10.1039/C6CP07897D